PAN POLSKA AKADEMIA NAUK

METROLOGY AND MEASUREMENT SYSTEMS

Index 330930, ISSN 0860-8229

www.metrology.pg.gda.pl

M&MS

NOISE AND OPTICAL SPECTROSCOPY OF SINGLE JUNCTION SILICON SOLAR CELL

Lubomir Skvarenina, Robert Macku

Brno University of Technology, Faculty of Electrical Engineering and Communications, Technicka 3058/10, 616 00 Brno, Czech Republic (✉ *skvarenina@phd.feec.vutbr.cz*, +420 541 146 009, *macku@feec.vutbr.cz*)

Abstract

Noise spectroscopy as a highly sensitive method for non-destructive diagnostics of semiconductor devices was applied to solar cells based on crystalline silicon with a view to evaluating the quality and reliability of this solar cell type. The experimental approach was used in a reverse-biased condition where the internal structure of solar cells, as well as *pn*-junction itself, was electrically stressed and overloaded by a strong electric field. This gave rise to a strong generation of a current noise accompanied by local thermal instabilities, especially in the defect sites. It turned out that local temperature changes could be correlated with generation of flicker noise in a wide frequency range. Furthermore, an electrical breakdown in a non-stable form also occurred in some specific local regions what created micro-plasma noise with a two-level current fluctuation in the form of a Lorentzian-like noise spectrum. The noise research was carried out on both of these phenomena in combination with the spectrally-filtered electroluminescence mapping in the visible/near-infrared spectrum range and the dark lock-in infrared thermography in the far-infrared range. Then the physical origin of the light emission from particular defects was searched by a scanning electron microscope and additionally there was performed an experimental elimination of one specific defect by the focused ion beam milling.

Keywords: non-destructive diagnostics, c-Si solar cells, $1/f$ noise, electroluminescence, lock-in IR thermography.

1. Introduction

Although the experimental examination of the *crystalline silicon* (c-Si) solar cells can be in principle applied to reverse/forward conditions, the nature of the observed noise (as well as light emission or thermal overheating) strongly depends on these conditions. In view of this fact, our study strictly differentiates the results obtained in a reverse/forward-bias condition [1]. Therefore, it should be noted that all results presented in this paper, with the exception of transport characteristics, were exclusively obtained in a reverse-bias condition. The similar research on noise fluctuations in the c-Si solar cells was provided by Z. Chobola [2] and J. Vanek [3]. The results of their research on noise fluctuations with a relation to defects in c-Si solar cells – also as our results – exhibit an inversely proportional dependency of the power spectral density on the frequency and directly proportional – on the square of an applied DC current at low injection

Article history: received on Dec. 31, 2015; accepted on Mar. 10, 2018; available online on Jun. 30, 2018, DOI: 10.24425/119565.

levels. The type of noise that exhibits this dependency is known as a flicker noise (or an f^{-1} noise) and its fundamental background was described in detail by F.N. Hooge [4]. In addition to the noise measurements, the research was simultaneously focused on the optical and thermal inspection of c-Si solar cells. It is based on publications of O. Breitenstein [5], P. Würfel [6] and D. Lausch [7], where the light emission is enforced by applying the reverse-bias in order to examine the pre-breakdown sites. The experimental arrangement for measurement of electroluminescence used in our research is similar to the imaging system used by M. Bliss [8]. The main difference of our approach to measurement is the use of filters to obtain spectrally-filtered electroluminescence.

2. Experimental details

The solar cells are generally fabricated from a wide variety of materials by using many different processing techniques. The set of samples used in this research were fragments of a single solar cell purposefully prepared by simple breaking it with a random dimension and a random angular orientation of corners. Preparation of smaller samples containing defects from solar cells is necessary to achieve high discrimination and categorization of particular defects. The newly prepared samples exhibit considerable initial instability. Therefore, artificial aging of samples is necessary to ensure repeatability of measurements.

The original solar cell was produced from a single-crystalline silicon wafer with a thickness of 125 μm and a size of (102 × 102) mm, 144 mm in diagonal with a surface area of 103 cm^2. The wafer was produced from a *p*-type substrate by the Czochralski process with a resistivity of 1.2 Ω·cm^2. Reduction of the surface reflectivity to improve the solar cell efficiency was achieved by etching of a pyramid texture and by coating of the nitride layer. The width of a depletion region without an applied bias voltage was approximately equal to 0.6 μm. The contacts were prepared with the screen printing technology from Ag paste on the near side, whereas the rear side had a structure of Al BSF with Ag/Al busbars [9].

2.1. Low-frequency noise spectroscopy

The experimental arrangement of an assembled system for low-frequency noise measurements is shown in Fig. 1. A sample was placed between two conductive aluminium electrodes into an electrically shielded dark environment in reverse-bias. An insulation outside the area of the sample was used to avoid a short circuit and a leakage effect. The constant excitation of the sample was achieved by applying a reverse-bias voltage from the output (0–25) V of an Agilent E3631A source. Additionally, a capacitor with a capacity of 2.2 μF at the input of the circuit was used to stabilize a voltage ripple and eliminate excess noise of the voltage source itself. The noise signal from the sample was sensed at the output of circuit terminated by a resistor and its resistance of 5.517 Ω was chosen to keep satisfactory proportion between noise sensitivity and noise floor. The sensed noise signal was amplified by an ultra-low-noise preamplifier Signal Recovery 5184 with a fixed voltage gain of ×1000 (60 dB) and a frequency response from 0.5 Hz to 1 MHz. The noise background of the amplifier was 800 pV·Hz$^{-1/2}$ at a frequency of 1 kHz. Finally, the noise signal was applied to the unbalanced input of a Rohde & Schwarz FMU36 baseband analyser (a measurable frequency band from 10 Hz to 36 MHz) with an optional impedance of 1 MΩ. The advantage of the analyser was its high sensitivity at low frequencies what enabled precise analysing of very weak signals. Despite this fact, it was necessary to use a preamplifier for a relatively high noise background of the analyser.

The low-noise version of double-shielded coaxial cable was used in the configuration to ensure sensing of the authentic noise signal. The apparatuses were interconnected via 8-bit standard IEEE-488.2 parallel bus GPIB (*General Purpose Interface Bus*) and then connected to the PC by an Agilent 82357B USB/GPIB converter interface (see Fig. 1). These instruments were programmed using text-based SCPI (Standard Commands for Programmable Instruments) commands through Instrument Control Toolbox in the MATLAB®.

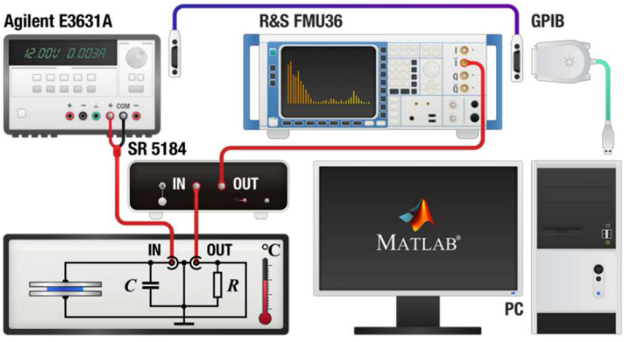

Fig. 1. The experimental configuration of a measurement system for registration of low-frequency noise fluctuations.

The dependence of *power spectral density* (PSD) on frequency $S_I(f)$ was examined in a spectral range from 10 Hz to 1 MHz. The lower-frequency limit of this range was affected by the specification of the analyser itself and the upper-frequency limit was affected by the frequency response of the amplifier. In any case, this limitation did not constitute any restriction for our experiments. The dependence of PSD on frequency was measured with several voltages, namely for voltages from 8 V to 15 V with an increment of 1 V. The current through the sample was negligibly small below this voltage interval and a long-term exposure to a strong electric field could cause damage to the sample above this voltage interval. The analysis of FFT-based spectrum for one value of voltage-bias was carried out in the measurable range for 120 points (24 points per frequency decade). The measurement of each point was performed for a centre frequency set within a span (a range between a start/stop frequency) of 10% on the logarithmic scale. The frequency span was changing in dependence on the centre frequency according to $\Delta f_{\text{span}} = 0.1 \cdot f_{\text{centre}}$. It should be noted here that the span of frequencies below 100 Hz was constantly set to 10 Hz. This was caused by the limited specification of the analyser itself which enabled to set the minimum span to 10 Hz for working in the frequency domain. After setting the span below 10 Hz the measurement was automatically switched to the time domain. Despite this limitation there were achieved very precise results in this very low-frequency range. The power spectral density for each point was calculated as a median of 625 measurement points from one trace which was obtained by averaging of 16 consecutive sweeps. This measurement approach significantly suppressed the influence of occurred noise spikes and ensured acquisition of true noise fluctuations' magnitude. The same approach was used to obtain the dependence $S_I(f)$ of PSD on the applied reverse current.

2.2. Spectrally-filtered electroluminescence and dark lock-in IR thermography

The experimental configuration for spectrally-filtered *electroluminescence* (EL) and *lock-in IR thermography* (DLIT) is shown in Fig. 2. Registration of enforced photon emission from

a reverse-biased *pn*-junction of c-Si solar cells was used for localization of defect-related sites in the form of light-emitting spots [10]. The sample was electrically contacted with a silver-plated finger contact on a horizontal *xy* plane with a linear travel length of (150 × 150) mm. This positioning plane was additionally equipped with stepper motors for remote control of both axes.

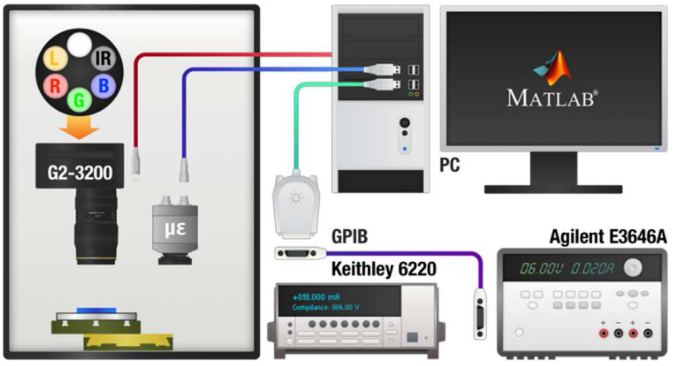

Fig. 2. The experimental setup for spectrally-filtered electroluminescence mapping and lock-in IR thermography.

Registration of light emission was ensured by a high sensitive *charge-coupled device* (CCD) camera G2-3200 remotely controlled by a stepper motor in the *z*-axis. It was necessary to place the device in a dark environment to avoid unwanted effects of external lighting. The CCD camera was equipped with a silicon chip KAF-3200ME (for quantum efficiency see Fig. 3) with a resolution of (2184 × 1472) pixels and a spectral response of (300–1100) nm. The Si sensor was constantly cooled by a dual system of Peltier modules with a typical operating temperature of 45°C below the ambient temperature to minimize the dark current. The dark current of the Si sensor at temperature of 0°C was 0.8 e·s^{-1} for a single pixel of (6.8 × 6.8) μm dimension and it was doubled after increasing the temperature to 6°C. The lens with a focal length of 41.7 mm

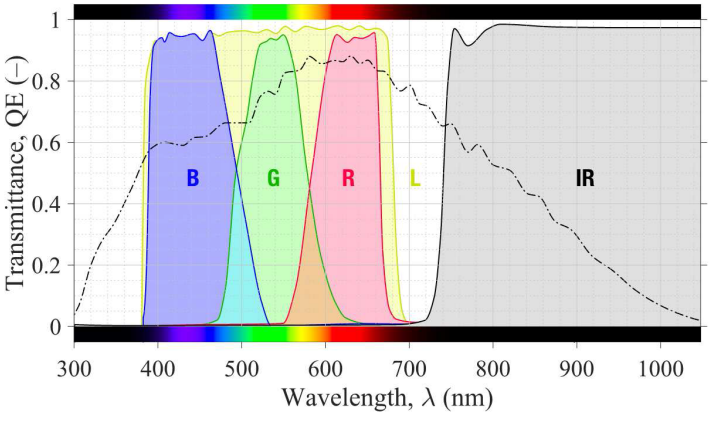

Fig. 3. Transmittance of installed IR, L-RGB filters (solid lines) in a carousel system with a quantum efficiency of monochrome Si sensor KAF-3200ME (dash-dot line), $\overline{\mathrm{QE}} = 0.528$, $\mathrm{QE}_{\max} = 0.882$ at $\lambda = 630$ nm.

and aperture of $f/1.2$ was used with the camera. The camera was additionally equipped with an automatic carousel system with six positions for standard 31.8 mm threaded filters. The filters installed into a carousel system were L-RGB type 2c and IR Pro 742.

Local overheating was registered by using the lock-in technique with a thermal imager $\mu\varepsilon$ TIM 160. This *infrared* (IR) camera was equipped with an uncooled micro-bolometer focal plane array detector with a resolution of (160×120) pixels and a response of (7.5–13) μm to the far-infrared spectral range. The periodically pulsed modulation was ensured by a Keithley 6220 current source for the dark IR lock-in technique. A *scanning electron microscope* (SEM) Tescan LYRA 3 was used for a micro-scale examination of the localized defects by the electroluminescence and lock-in IR thermography. The experimental modification of specific defects was performed by the *focused ion beam* (FIB) milling with Ga ions.

3. Results and discussion

The current density-voltage $(J{-}V)$ characteristic of a sample marked as M is shown in Fig. 4a. The measurements of transport characteristic are very useful for detection of local/global breakdowns, especially in a reverse-bias condition [11]. As can be seen in Fig. 4a, the $J{-}V$ characteristic is a smooth function in a reverse/forward-bias without any observable bias-induced breakdowns or another non-stable form of current conduction. However, the invariable/time-independent local breakdowns are not an obstacle for the noise measurement but it is essential to choose an applied voltage-bias in the stable part of reverse $J{-}V$ characteristics. The reverse $J{-}V$ characteristic in Fig. 4a is linear and resistive-like below the voltage of 0.1 V. Above this voltage the curve is partly non-linear and its slope changes due to imperfections in the structure of c-Si sample [12]. Also, the low-ohm component caused by the defects (they behave as low-resistive paths) became more dominant above the voltage of 2.5 V. The basic parameters from the transport characteristic in Fig. 4a were determined by fitting/interleaving the experimental data by a single-diode model with the Lambert-W function [13]. It should be noted here that a double-diode model for c-Si solar cells is commonly used in our experiments. However, the use of a single-diode model for the sample M proved to be sufficient [14, 15]. The parameters extracted with experimental and fitted data are shown in Fig. 4b. The obtained ideality factor of

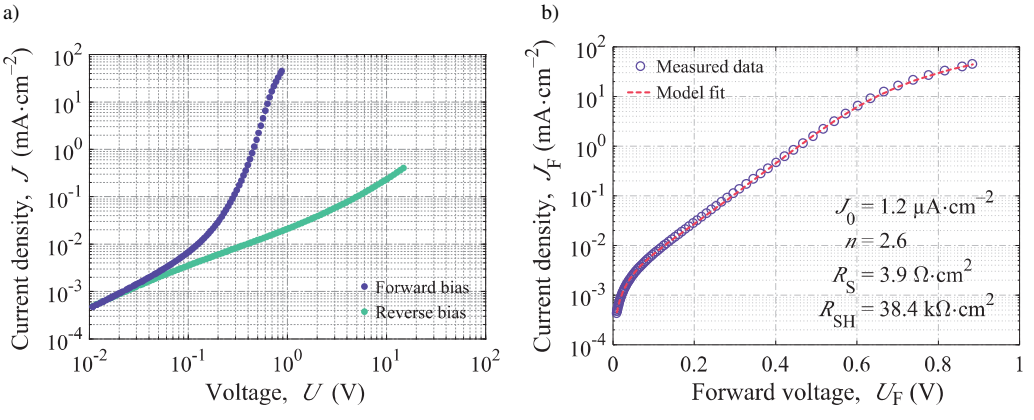

Fig. 4. An experimental dark forward/reverse $J{-}V$ characteristic in the log-log scale (a); experimental forward $J{-}V$ characteristics (empty circles) in the semi-log scale, simulated $J{-}V$ (dashed line) with equivalent parameters after approximation by a single-diode model with the Lambert-W function (b), c-Si sample M, maintained $T = 298.15$ K.

$n = 2.6$ for the sample M can be interpreted as the predominant conductivity of recombination current through defect states, *i.e.* recombination states. The ideality factor greater than two is due to extended defects at the edges or other defects in the area of the sample. The ideality factor of $J-V$ characteristics is smaller than two ($n < 2$) if the defects have a low local density of the defect states and then behave according to the Shockley-Read-Hall recombination theory of isolated point defects. On the contrary, the ideality factor can be greater than two ($n > 2$) if the defects have a high local density of the defect states and they are accompanied with a multi-level recombination which may show an intrinsic saturation behaviour [16].

The experimental results of noise spectral densities with an increasing value of the applied voltage are shown in Fig. 5a. With the approach described in Section 2 the noise measurements are significantly time-consuming; they take about 12 hours (1.5 hours for one PSD). Therefore, it has proved to be essential to maintain constant conditions (*e.g.* the ambient temperature) throughout the measurement period. Also, the repeatability of the measurement and the time independence of the results were verified by measuring the PSD eight times for the applied voltage of 8 V. The noise floor in Fig. 5a is related to the excess noise produced by the experimental apparatuses alone. The spectral analysis in Fig. 5a shows that the current noise power spectral density has the form of f^{-1} noise (flicker noise). This type of noise is the dominant noise in the low-frequency range and it is present in all semiconductor devices under biasing [17]. The inversely proportional dependence of power spectral density on frequency can be generally expressed as $S_I(f) \sim f^{-\gamma}$, where $\gamma \approx 1$. The power spectral density of sample M shows proportionality to the frequency of $0.95 \leq \gamma \leq 1.19$ for the applied voltage of (8–15) V. Nevertheless, this PSD dependence is valid for $f < 8$ kHz at $U_R = 8$ V, and for $f < 4$ kHz at $U_R = 15$ V. Above these frequencies, the inversely proportional dependences are affected by non-specific additive components. These additive components can generally be expressed in the form of Lorentzian-noise spectra [18]. The exact origin of flicker noise is still not sufficiently clarified in general but it is usually assumed that the f^{-1} noise is a result of bulk imperfections in a crystal lattice [19]. This assumption is based on the Hooge's bulk model where only scattering the carrier on the silicon crystal lattice alone leads to pronounced f^{-1} noise during the carrier transport and scattering from the impurity ions does not influence the level of noise fluctuations [20]. Nevertheless, some

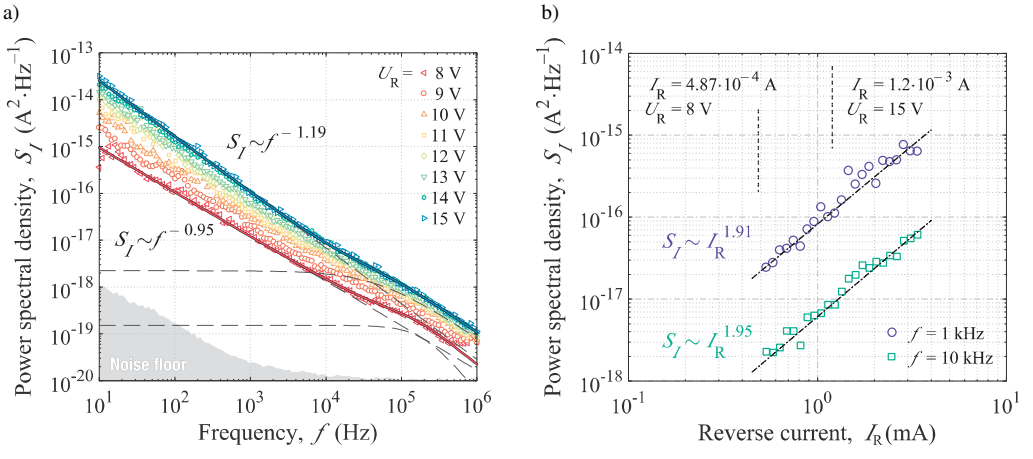

Fig. 5. Noise power spectra as functions of frequency $S_I(f) \sim f^{-\gamma}$, applied $U_R = \{8, 9, \ldots, 15\}$ V, solid lines indicate the approximated superposition of noise components (denoted by dashed lines) (a); noise power spectra vs. reverse current $S_I(f) \sim f^{\beta}$, taken at $f = \{1, 10\}$ kHz, (dash-dot lines denote current dependence, dashed lines denote the equivalent reverse current to the reverse voltage 8–15 V) (b); c-Si sample M, ambient $T = 298.15$ K.

experimental results exhibit a strong influence of the surface [21]. The Hooge's bulk model of the f^{-1} (flicker) noise is described by an empirical relation for homogeneous non-degenerate semiconductors:

$$\frac{S_I(f)}{I^2} = \frac{\alpha_{\mathrm{H}}}{fN}, \tag{1}$$

where $S_I(f)$ is a PSD related to fluctuations of current; I is a direct current; α_{H} is a dimensionless constant known as the Hooge's constant; f is a frequency and N is the total number of free carriers participating in the fluctuation process [22]. However, from (1) it is possible to express a measurable quantity which is defined as a noise quality and reliability indicator C_{Q} according to [23]. This quantity is given as the ratio of the Hooge's constant and the total number of fluctuating charge carriers $C_{\mathrm{Q}} = \alpha_{\mathrm{H}} N^{-1}$. Then the power spectral density of the f^{-1} noise current in respect of (1) may be written as $S_I = C_{\mathrm{Q}} I^2 f^{-1}$. Therefore, the deviation of noise spectra in Fig. 5a from the authentic behaviour of f^{-1} type noise may be generally approximated by the superposition of separate noise components:

$$S_I(f) = \underbrace{C_{\mathrm{Q}} \frac{I^{\beta}}{f^{\gamma}}}_{\text{Flicker}} + \underbrace{\sum_{i=1}^{n} \frac{S_{0_i}}{1 + (f/f_{c_i})^{\delta}}}_{\text{Lorentzian}} + \underbrace{\frac{4\mathrm{k_B}T}{R}}_{\text{Thermal}}, \tag{2}$$

where the f_c is a corner frequency; S_0 is a plateau value of PSD which is frequency independent for $f < f_c$ and proportional to $f^{-\delta}$ for $f > f_c$, β, γ and δ are constants ($\beta \approx 2$, $\gamma \approx 1$ and $\delta \approx 2$); $\mathrm{k_B}$ is the Boltzmann constant; T is temperature and R is an equivalent resistance. It is obvious from (2) that the noise quality indicator C_{Q} is dimensionless only if $\beta = 2$ and $\gamma = 1$ [24]. The estimated parameters of the flicker noise component from measured spectra $S_I(f)$ in Fig. 5a are $C_{\mathrm{Q}} = (4.00 \pm 0.15) \cdot 10^{-8}$ at $U_{\mathrm{R}} = 8$ V with a slope of $\gamma = 0.95$ and $C_{\mathrm{Q}} = (2.64 \pm 0.06) \cdot 10^{-7}$ at $U_{\mathrm{R}} = 15$ V with a slope of $\gamma = 1.19$. The apparent deviation above $f > 8$ kHz for PSD of $U_{\mathrm{R}} = 8$ V is obtained by adding the Lorentzian component (the dashed line in Fig. 5a) with extracted parameters $S_0 = 1.5 \cdot 10^{-19}$ A^2·Hz^{-1} and $f_c = 200$ kHz. The authentic f^{-1} noise with the applied voltage of $U_{\mathrm{R}} = 15$ V in Fig. 5a is influenced by the sum of several superimposed Lorentzian components above $f > 4$ kHz. The dependence of noise power spectral densities on the applied reverse current in Fig. 5b is examined at $f = 1$ kHz and $f = 10$ kHz. The dependence of PSD on the reverse current in Fig. 5b should exhibit direct proportionality to the square $S_I(f) \sim I^{\beta}$, where $\beta \approx 2$ [25]. The power spectral density in Fig. 5b shows proportionality to the current of $1.91 \leq \beta \leq 1.95$ at frequencies of 1 kHz and 10 kHz. The evaluated noise quality indicators from the measurement in Fig. 5b are $C_{\mathrm{Q}} = (5.0 \pm 0.5) \cdot 10^{-8}$ at $f = 1$ kHz with a slope of $\beta = 1.91$ and $C_{\mathrm{Q}} = (4.8 \pm 0.3) \cdot 10^{-8}$ at $f = 10$ kHz with a slope of $\beta = 1.95$. At lower frequencies other types of noise (micro-plasma or shot noise) may be present, however, they are apparently masked by the dominant f^{-1} type noise. It should be noted here that the noise results in Fig. 5b are acquired independently from the results in Fig. 5a.

Localization of an individual microstructural defect in a macro scale is achieved by electrically excited light emission from a reverse-biased *pn*-junction. The intensity of the light emission in Fig. 6 is expressed as a *photon flux* (Φ_{q}) in photons per second. As can be seen in the *electroluminescence* (EL) map of the whole sample in Fig. 6a, the defect-related light emission is mainly concentrated at the edges (some is also in the sample volume) in the form of spot-oriented light distribution. It should be noted that an inappropriately prepared edge would radiate along its entire length, not in the form of locally distributed light spots. These areas with localized light spots are heavily stressed in comparison with the rest of the *pn*-junction. In respect of our previous research, we suppose that the stressed local areas contributed to the formation of excessive

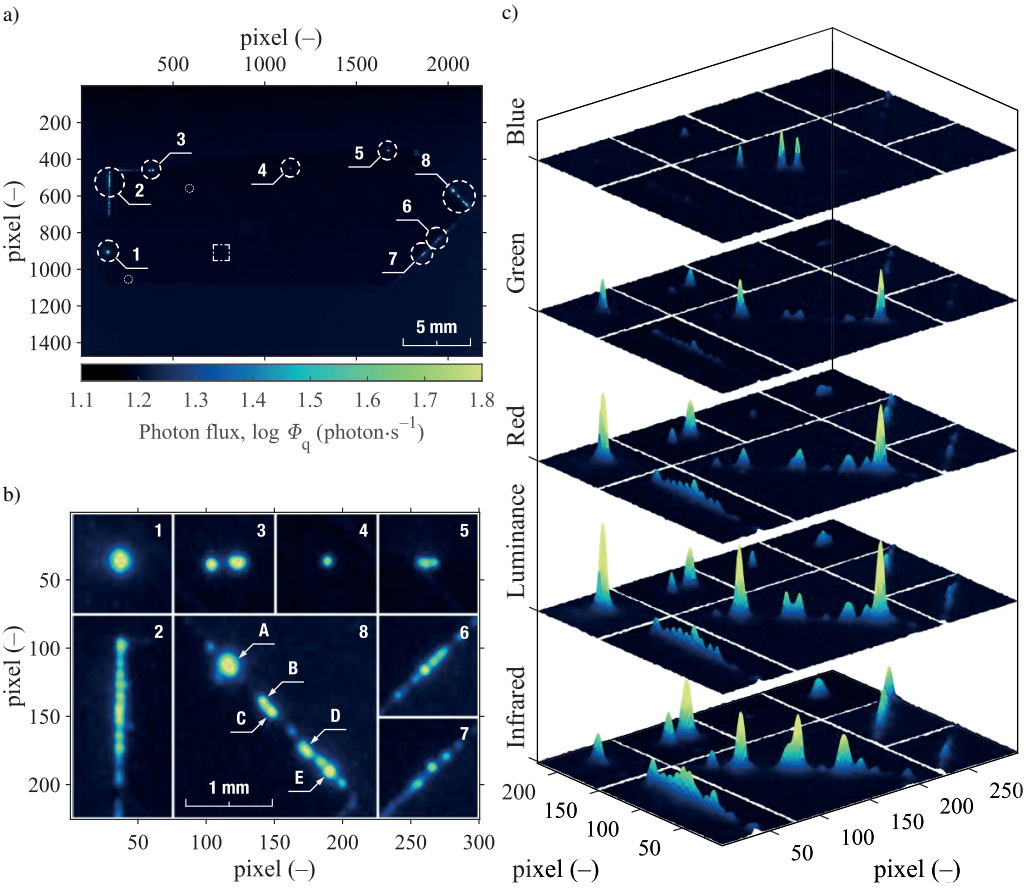

Fig. 6. An electroluminescence map with active defect-related light spots, *regions of interest* (ROI's) marked by dashed circles (a); a close-up view of marked ROIs with defect-related light emission without an applied filter, specific defects denoted by arrows (b); ROIs with corresponding IR, L-RGB filter in a 3D view for simpler spatial comparison (c); integration time 300 s, c-Si sample M, area 225 mm^2, $I_R = 4$ mA, ambient $T = 299.15$ K.

noise fluctuations [26]. Generally, the intensity of light spots associated with the defects will increase with the reverse bias increase, but also the number of light spots may increase where defect-related sites become active at some certain level of a reverse bias. Therefore, additional information about the nature of defect-related sites may be achieved by measuring the light intensity at different reverse bias [27]. Selected *regions of interest* (ROIs) in Fig. 6a (marked by dashed circles) are shown in numbered close-up views in Fig. 6b. The electroluminescence in Figs. 6a, 6b is captured without applying any filter, therefore, the transmittance is limited only by the quantum efficiency of the Si-chip itself. Finally, the spectrally-filtered electroluminescence of the localized defect-related sites with a corresponding filter (see Fig. 3) is shown in a close-up 3D view in Fig. 6c. The dark *lock-in IR thermogram* (DLIT) of obtained areas, prone to overheating, is shown in Fig. 8. Moreover, after localization of defect-related sites by EL and DLIT in a macro scale, there is additionally performed a micro-scale exploration of the sample M by SEM. Then the detailed micrographs of a physical origin of localized defect-related light spots (Fig. 6) are shown in Fig. 9. Comparing the visible and near-infrared electroluminescence in

Fig. 6c it is obvious that not all defect-related light spots radiate with higher intensity in the near-infrared spectrum. Specifically, the defect-related light spots 1 and 8A exhibit higher intensity in the visible spectrum and, in addition, the spot 8E absolutely does not radiate in the near-infrared spectrum. The light intensity may have a peak at a different wavelength due to a different origin of the electroluminescence process [28], *e.g.* in the band-to-band radiative recombination, trap-assisted recombination (impurities or mechanically induced defects), impact-ionization assisted avalanche emission [29, 30].

As can be seen in Fig. 7, simple discrimination (as categorization) of the localized light spots can be made by normalization of light intensity into a pseudo-colour image. The electroluminescence captured by using RGB filters (in Fig. 6a) is simply assigned to RGB channels with an 8-bit colour depth. This basic approach with a restriction to the visible spectrum makes possible to differentiate particular defects among themselves on the basis of a predominant colour in the pseudo-color image. Then the light emission associated with defect 1 appears as a red spot, 8A as a green spot, 8B as a blue spot, 8C as a purple spot and 8E as a yellow spot (compare Fig. 6 and Fig. 7). The thermal radiation, expressed as a *temperature difference* (ΔT) of the whole sample in Fig. 8, increased by applying a reverse bias and three areas prone to overheating has appeared in the thermogram. The first thermal area marked by a dash-dot square in Fig. 8 is related to a very weak light emission glow from a defect-site under a third busbar (below a finger contact) in Fig. 6a. The light emission around a busbar is almost undetectable (in Fig. 6a, more visible in Fig. 10) due to the simple fact that the light emission cannot directly penetrate a metal. The second area most prone to local thermal overheating in the top-left corner (see Fig. 8) may be associated with a defect-related ROI 2 in Fig. 6 but the light emission is not so significant compared with other defect-related ROI's. However, the defect area 2 in Fig. 9a exhibits an undefined structure (may be a residue of the metallization process; the EDS analysis will be performed) on the surface near the edge which may be an originator of strong thermal overheating in this area [31]. The last area prone to overheating in the right part of the sample may be associated with defect-related ROI 6 in Fig. 6 but the thermal distribution is uniform along the edge from the seventh busbar to the middle corner.

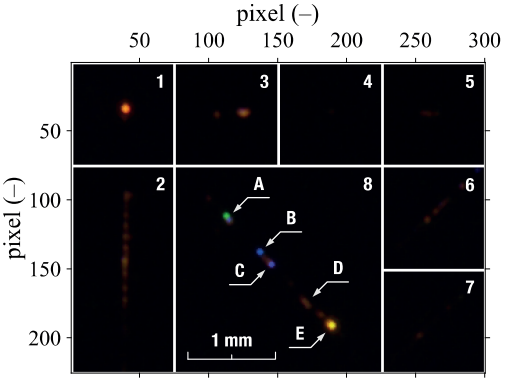

Fig. 7. ROIs in the pseudo-color representation obtained by a combination of normalized photon flux of particular RGB filters to RGB channels.

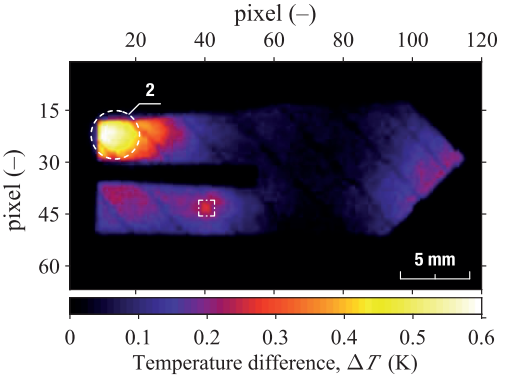

Fig. 8. A lock-in thermogram, distribution of local overheating, $f_{\text{lock-in}} = 250$ mHz, $n = 100$, $I_{\text{R}} = 4$ mA, c-Si sample M, area 225 mm^2, ambient $T = 300.15$ K.

The experimental elimination of the defects influence on the electrical/optical measurements can be based on different approaches to the modification of solar cell structure by a *focused*

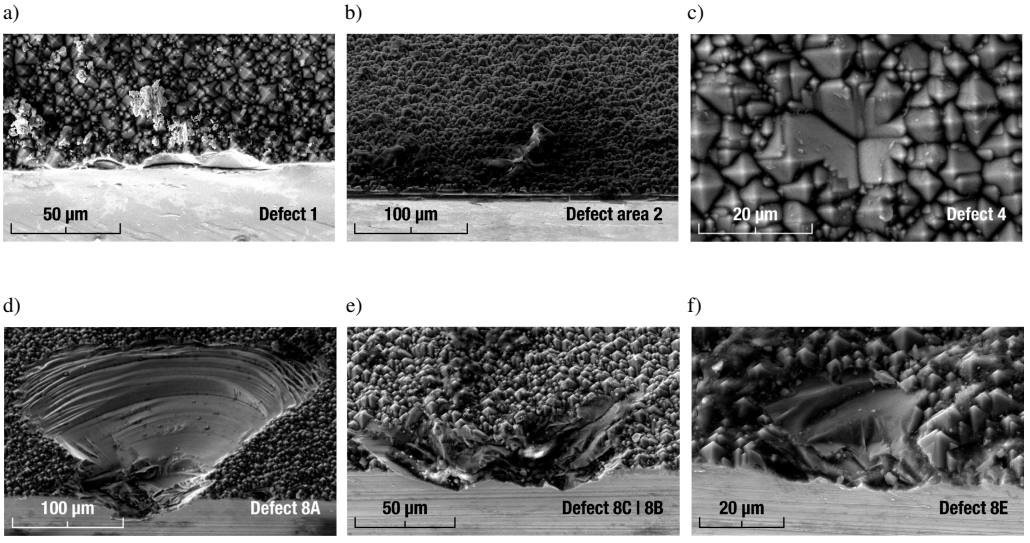

Fig. 9. The real structure of defects under the scanning electron microscope, a physical origin of defect-related spot light emission localized by the spectrally filtered electroluminescence and lock-in IR thermography, a defect on the edge, tilt 5° (a); a structure at the surface close to the edge, tilt 45° (b); a non-uniformity in the pyramid structure on the surface, tilt 0° (c); a defect on the edge, tilt 35°, c-Si sample M, accelerating voltage 15 kV, detector SE (d, e, f).

ion beam (FIB). The first approach may be based on isolating the defects from the rest of the *pn*-junction by a barrier. The depth/width of the barrier set for individual defects should be as small as possible to achieve the smallest modification of the surrounding area in order to avoid creation of additional recombination centres. The second approach is based on a modification of the defect itself where only the defect-related area is completely evaporated by the FIB. It should be noted that the experimental milling by FIB may create additional recombination centres and the intended elimination of a defect may not be successful at all (the FIB also causes implantation of Ga ions into a c-Si structure). Anyway, the area of the solar cell structure modified by the barrier is larger than the area modified by evaporation of the defect itself. Therefore, the experimental elimination is based on simple evaporation of a defect-related microstructure. The experimental modification is performed for defect 1 (Fig. 9a) which is accompanied with the strongest defect-related light emission in the visible spectrum (highest amplitude of a light emission captured by the luminance filter, see Fig. 6). As can be seen in Fig. 9, the physical structure of defect 1 (Fig. 9a) is also quite different in comparison with other defects at the edge (Figs. 9d, 9e, 9f). The impact of the experimental modification is reflected in an additional electroluminescence map shown in Fig. 10 and the low-frequency noise measurement shown in Fig. 11. The light spot on the edge of the sample clearly disappeared (denoted by a green dashed circle in Fig. 10) and defect-related light emission became undetectable in the visible and near-infrared spectrum. The SEM detail of defect-related edge after the FIB milling is also shown in Fig. 10. The defects may be generally considered as alternative parallel low-resistance paths for the reverse current. Therefore, the current flow through other defects slightly increased after the elimination of defect 1 what led to an increase of radiation intensity (see Fig. 10) at the same applied reverse bias. The edge defect 1 does not participate in the local thermal overheating (see Fig. 8), so the thermography after modification does not provide any further information. The comparison of noise spectra before and after FIB milling is shown in Fig. 11. The original noise spectra (red

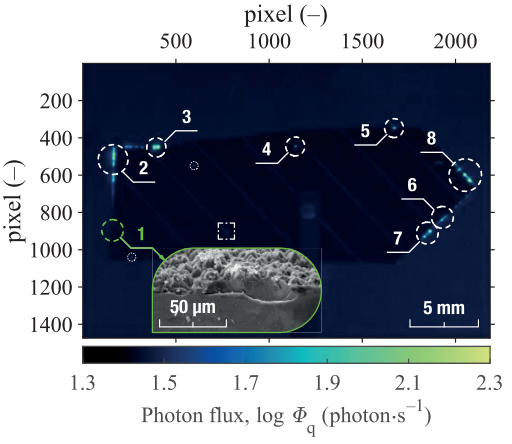

Fig. 10. Electroluminescence after the experimental elimination of the localized defect 1 by focused ion beam milling, the SEM detail of the edge after milling, tilt 55°, c-Si sample M, ambient $T = 301.15$ K.

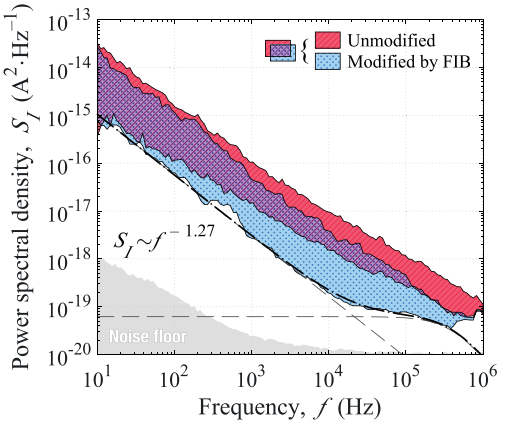

Fig. 11. Comparison of the current noise power spectra before (line fill pattern) and after (dot fill pattern) the experimental elimination of the localized defect 1 on the edge, c-Si sample M, ambient $T = 298.15$ K.

line fill) from Fig. 5a and the modified noise spectra (blue dot fill) are plotted as areas in Fig. 11 for a visible comparison of changes in PSD (purple dot-line fill denotes an overlap of PSD). The lower/upper limits of these areas are related to the applied reverse voltage (8–15) V, as in Fig. 5a. The parameters, according to (2), of the flicker noise component, extracted from the modified PSD are $C_Q = (9.0 \pm 0.5) \cdot 10^{-8}$ at $U_R = 8$ V with a slope of $\gamma = 1.27$, and the estimated parameters of additive Lorentzian component are $S_0 = 6 \cdot 10^{-20}$ A^2·Hz^{-1}, $f_c = 400$ kHz. Although the quality indicator C_Q is ~ 2.25 times higher for $U_R = 8$ V after the FIB milling, the total power spectral density with an increasing frequency decreases with a steeper slope of $\Delta\gamma = 0.32$. The $J-V$ characteristics after the elimination of defect 1 are also evaluated (not presented here) but the change after comparison of $J-V$ curves is almost imperceptible. Therefore, the f^{-1} noise can be considered as a significantly more sensitive tool for the quality assessment of semiconductors (as well as other electronic devices, *e.g.* supercapacitors [32]) than the observation of changes in ordinary $J-V$ characteristics [33].

4. Conclusion

This paper presents a comprehensive study of c-Si solar cells with a focus on the examination of microstructural defects. The examination of low-frequency noise showed that the excess noise at different reverse bias is regularly in the form of the f^{-1} (flicker) noise. Specifically, the average slope of measured PSD dependence $S_I(f) \sim f^{\gamma}$ was estimated from the Hooge's equation to be $\gamma = 1.07 \pm 0.12$ for $U_R = (8-15)$ V. Furthermore, the deviation from the authentic f^{-1} noise at higher frequencies was approximated by the superposition of additional Lorentzian components. The examination of spectrally-filtered electroluminescence showed the emission of photons in the form of locally distributed light-spots related to microstructural defects. This defect-related light emission was possible to be distinguished on the intensity basis not only in the visible/near-infrared spectrum but also in the visible spectrum itself. Moreover, it also succeeded in finding

the physical origin of defects in a microscale which was responsible for the occurrence of light emission.

Subsequently, the research was aimed at the experimental elimination of localized microstructural defects which were identified in a micro scale as the physical origin of defect-related light emission. This experimental elimination by FIB milling was performed for one specific defect which exhibited the strongest light emission in the visible spectral range. The results obtained after the experimental milling process confirmed a successful elimination of the defect influence. The original defect-related light emission became undetectable in the visible/near-infrared spectral range after FIB milling and the excess noise in the low-frequency PSD measurement significantly decreased. Although the noise quality indicator C_Q increased from $4 \cdot 10^{-8}$ to $9 \cdot 10^{-8}$, the total excess noise decreased with a steeper slope of $\gamma = 1.25$ for $U_R = 8$ V (the original slope was less steep by $\Delta\gamma = 0.32$ at the same reverse bias). The observed difference in slope may be considered as a change in the nature of the f^{-1} noise.

The further research will continue to monitor the changes in noise measurements after a progressive elimination of remaining localized defects accompanied with light emission in the electroluminescence map by experimental FIB milling.

Acknowledgments

The research presented in this paper was financed by the Internal Grant Agency of Brno University of Technology, grant No. FEKT-S-17-4626 and by the National Sustainability Program under grant LO1401. In the research, the infrastructure of the SIX Centre was used.

References

[1] Macku, R., Sicner, J., Dallaeva, D. (2012). An experimentally based characterization of solar cell structure defects by means of noise and optical activities analysis. *Fracture Mechanics for Durability, Reliability and Safety*., 499–506.

[2] Chobola, Z. (2001). Noise as a tool for non-destructive testing of single-crystal silicon solar cells. *Microelectron. Reliab*., 41(12), 1947–1952.

[3] Vanek, J., Dolensky, J., Chobola, Z., Lunak, M., Poruba, A. (2012). Low Frequency Noise and Microplasma Analysis for c-Si Solar Cell Characterization. *Int. J. Photoenergy*, 5.

[4] Hooge, F.N., Kleinpenning, T.G.M., Vandamme, L.K.J. (1981). Experimental studies on $1/f$ noise. textitRep. Prog. Phys., 44(5), 479–532.

[5] Breitenstein, O., Bauer, J., Trupke, T., Bardos, R.A. (2008). On the detection of shunts in silicon solar cells by photo- and electroluminescence imaging. *Prog. Photovolt. Res. Appl*., 16(4), 325–330.

[6] Wurfel, P., Trupke, T., Puzzer, T., Schaffer, E., Warta, W., Glunz, S. W. (2007). Diffusion lengths of silicon solar cells from luminescence images. *J. Appl. Phys*., 101, 123110.

[7] Lausch, D., Petter, K., Wenckstern, H., Grundmann, M. (2009). Correlation of pre-breakdown sites and bulk defects in multicrystalline silicon solar cells. *Phys. Stat. Sol. RRL*, 3, 70–72.

[8] Bliss, M., Wu, X., Bedrich, K.G., Bowers, J.W., Betts, T.R., Gottschalg, R. (2015). Spatially and spectrally resolved electroluminescence measurement system for photovoltaic characterisation. *IET Renewable Power Generation*, 9(5), 446–452.

[9] Koktavy, P., Macku, R. (2011). Noise and Optical Activities of Local Defects in Solar Cells pn Junctions. *21st Int. Conf. on Noise and Fluctuations*, Toronto, 405–408.

[10] Bishop, J.W. (1989). Microplasma Breakdown and Hot-spots in Silicon Solar Cells. *Solar Cells*, 26, 335–349.

[11] Macku, R., Koktavy, P. (2009). Improved electrical characterization of silicon solar cells based on noise spectroscopy in forward direction. *Proc. 24th European Photovolt. Solar Energy Conf.*, Hamburg: WIP Renewable Energies, 484–488.

[12] Levinshtein, M., Kostamovaara, J., Vainshtein, S. (2005). *Breakdown Phenomena in Semiconductors and Semiconductor Devices*. London: World Scientific.

[13] Romero, B., Del Pozo, G., Arredondo, B. (2012). Exact analytical solution of a two diode circuit model for organic solar cells showing S-shape using Lambert W-functions. *Solar Energy*, 86, 3026–3029.

[14] Batzelis, E., Papathanassiou, S. (2015). A method for the analytical extraction of the single-diode PV model parameters. *IEEE Transactions on Sustainable Energy*, 7(2), 1–9.

[15] Jammadi, M., Merrikh-Bayat, F., Bigdeli, M. (2016). Very accurate parameter estimation of single- and double-diode solar cell models using a modified artificial bee colony algorithm. *Int. J. Energy Enviromental Engineering*, 7(1), 13–25.

[16] Breitenstein, O., Altermatt, P., Ramspeck, K., Schenk, A. (2006). The Origin of Ideality factors $n > 2$ of Shunts and Surfaces in the Dark I-V Curves of Si Solar Cells. *Proc.of the 21st Europ. Photovol. Solar Energy Conf.,* Dresden, 21, 625–628.

[17] Konczakowska, A., Wilamowski, B. (2011). Noise in Semiconductor Devices. *Fundamentals of Industrial Electronics*, Electrical Engineering Handbook, CRC Press, 1–12.

[18] An, Y., Rao, H., Bosman, G., Ural, A. (2012). Random telegraph signal and $1/f$ noise in forward-biased single-walled carbon nanotube film-silicon Schottky junctions. *Appl. Phys. Lett.*, 100(21), 2131021–4.

[19] Macku, R., Koktavy, P. (2010). Analysis of fluctuation processes in forward-biased solar cells using noise spectroscopy. *Phys. Stat. Sol.*, 207(10), 2387–2394.

[20] Hooge, F.N. (1969). $1/f$ Noise is no surface effect. *Physics Letters (A)*, 29, 139–140.

[21] Vandamme, L.K.J. (1994). Noise as a diagnostic tool for quality and reliability of electronic devices. *IEEE Trans. Elec. Dev.*, 41(11), 2176–2187.

[22] Hooge, F.N. (1994). 1/f noise sources. *IEEE Trans. Elec. Dev.*, 41(11), 1926–1935.

[23] Sikula, J., Schauer, P., Vasina, P., Sikulova, M., Koktavy, B., Chobola, Z., Navarova, H., Pazdera, L. (1994). $1/f$ Noise in metallic thin films. *AIP Conf. Proc.*, 371, 59–64.

[24] Dutta, P., Horn, P.M. (1981). Low-frequency fluctuations in solids: $1/f$noise. *Rev. Mod. Phys.*, 53(3), 497–516.

[25] Granqvist, C.G., Green, S., Jonson, E.K., Marsal, R., Niklasson, G.A., Roos, A., Topalian, Z., Azens, A., Georen, P., Karmhab, R., Smulko, J., Kish, L.B. (2008). Electrochromic foil-based devices: Optical transmittance and modulation range, effect of ultraviolet irradiation, and quality assessment by $1/f$ current noise. *Thin Solid Films*, 516(17), 5921–5926.

[26] Macku, R., Koktavy, P., Sicner, J. (2012). Comprehensive Study of Solar Cell Structure Defects by Means of Noise and Light Emission Analysis. *Advances in Electrical and Electronic Engineering*, 10(2), 130–135.

[27] Skarvada, P., Tomanek, P., Koktavy, P., Macku, R., Sicner, J., Vondra, M., Dallaeva, D., Smith, S., Grmela, L. (2014). A variety of microstructural defects in crystalline silicon solar cells. *App. Surf. Science*, 312, 50–56.

[28] Schneemann, M., Helbig, A., Kirchartz, T., Carius, R., Rau, U. (2010). Reverse biased electroluminescence spectroscopy of crystalline silicon solar cells with high spatial resolution. *Physica Status Solidi (A)*, 207, 2597–2600.

[29] Bothe, K., Ramspeck, K., Hinken, D., Schinke, C., Schmidt, J., Herlufsen, S., Brendel, R., Bauer, J., Wagner, J.M., Zakharov, N., Breitenstein, O. (2009). Luminescence emission from forward- and reverse-biased multicrystalline silicon solar cells. *J. of Appl. Phys*., 106(10), 104510.

[30] Brenstein, O., Bauer, J., Bothe, K., Kwapil, W., Lausch, D., Rau, U., Schmidt, J., Schneemann, M., Schubert, M.C., Wagner, J.M., Warta, W. (2011). Understanding junction breakdown in multicrystalline solar cells. *J. of App. Physics*, 109(7), 071101.

[31] Breitenstein, O., Bauer, J., Altermatt, P., Ramspeck, K. (2010). Influence of Defects on Solar Cell Characteristics. *Solid State Phenomena*, 156–158, 1–10.

[32] Szewczyk, A., Lentka, Ł., Smulko, J., Babuchowska, P., Beguin, F. (2017). Measurements of flicker noise in supercapacitor cells. *24th Int. Conf. on Noise and Fluctuations*, Vilnius, 1–4.

[33] Jones, B.K. (2002). Electrical noise as a reliability indicator in electronic devices and components. *IEE Proc. Circuits, Devices and Syst.*, 149(1), 14–22.